On magnetic field amplification and particle acceleration near non-relativistic astrophysical shocks: particles in MHD cells simulations

Allard Jan van Marle, Fabien Casse, Alexandre Marcowith

Monthly Notices
of the
ROYAL ASTRONOMICAL SOCIETY

MNRAS **473,** 3394–3409 (2018)
Advance Access publication 2017 September 27

doi:10.1093/mnras/stx2509

On magnetic field amplification and particle acceleration near non-relativistic astrophysical shocks: particles in MHD cells simulations

Allard Jan van Marle,[1]★ Fabien Casse[1] and Alexandre Marcowith[2]

[1]*Laboratoire AstroParticle and Cosmologie (APC), Université Paris Diderot, CNRS/IN2P3, CEA/Irfu, Observatoire de Paris, Sorbonne Paris Cité, 10 rue Alice Domon et Leonie Duquet, F-75205 Paris Cedex 13, France*
[2]*Laboratoire Univers et Particules de Montpellier (LUPM) Université Montpellier, CNRS/IN2P3, CC72, place Eugène Bataillon, F-34095 Montpellier Cedex 5, France*

Accepted 2017 September 25. Received 2017 September 25; in original form 2017 June 24

ABSTRACT

We present simulations of magnetized astrophysical shocks taking into account the interplay between the thermal plasma of the shock and suprathermal particles. Such interaction is depicted by combining a grid-based magnetohydrodynamics description of the thermal fluid with particle in cell techniques devoted to the dynamics of suprathermal particles. This approach, which incorporates the use of adaptive mesh refinement features, is potentially a key to simulate astrophysical systems on spatial scales that are beyond the reach of pure particle-in-cell simulations. We consider in this study non-relativistic shocks with various Alfvénic Mach numbers and magnetic field obliquity. We recover all the features of both magnetic field amplification and particle acceleration from previous studies when the magnetic field is parallel to the normal to the shock. In contrast with previous particle-in-cell-hybrid simulations, we find that particle acceleration and magnetic field amplification also occur when the magnetic field is oblique to the normal to the shock but on larger time-scales than in the parallel case. We show that in our simulations, the suprathermal particles are experiencing acceleration thanks to a pre-heating process of the particle similar to a shock drift acceleration leading to the corrugation of the shock front. Such oscillations of the shock front and the magnetic field locally help the particles to enter the upstream region and to initiate a non-resonant streaming instability and finally to induce diffuse particle acceleration.

Key words: astroparticle physics – MHD – plasmas – shock waves – methods: numerical.

1 INTRODUCTION

Cosmic rays (CRs) with energies between a few GeV to hundreds of PeV are produced in our Galaxy. One of the preferred ways to accelerate CRs is through repeated crossings of the particles across a shock front carrying magnetic fluctuations responsible for particle scattering (Drury 1983). This process is known as diffusive shock acceleration (DSA). It appears that energetic particles (shorten as CRs hereafter) can be accelerated so efficiently that they can drive their own magnetic fluctuations and sustain the acceleration process (Bell 1978). DSA can become so efficient that CR pressure modifies the shock structure and the acceleration process requiring non-linear CR back-reaction calculations to derive self-consistent solutions (Berezhko & Ellison 1999). It appears that CRs are also able to generate intense magnetic fields at fast shock fronts. This may provide an explanation for the high magnetic field strengths deduced from high angular resolution observations in the X-ray domain in several historical supernova remnants (SNRs) (Parizot et al. 2006). In fast shocks that prevail in young SNRs the streaming of CRs ahead the shock front triggers a class of plasma instabilities that can grow fast enough to produce magnetic field strengths sometimes in excess of the standard interstellar values (Zachary & Cohen 1986; Lucek & Bell 2000; Bell 2004) by several orders of magnitude. In particular, Bell (2004, 2005) shows that the fastest instability is induced by the return background plasma current that compensates the current produced by streaming CRs. Contrary to its kinetic equivalent, this instability is non-resonant and can be treated using ideal magnetohydrodynamics (MHD). The non-resonant streaming (NRS) instability has been tested in a long series of numerical studies using various techniques going from pure MHD (Zirakashvili, Ptuskin & Völk 2008), dihybrid (CRs and protons are treated by particle-in-cell or PIC methods and electrons as a fluid; Riquelme & Spitkovsky 2010; Caprioli & Spitkovsky 2014a) to Vlasov or PIC–MHD (Reville et al. 2008; Reville & Bell 2013; Bai et al. 2015); see Marcowith et al. (2016) for a review. The study by Bai et al. (2015) combines a kinetic description of CRs based on PIC methods coupled to a

★ E-mail: vanmarle@apc.univ-paris7.fr

MHD code that calculate the background magnetized fluid distribution.

Reville & Bell (2012, 2013) used 2D and then 3D simulations to investigate a CR-driven filamentation instability that also results from the onset of upstream CR streaming but contrary to the NRS generates long-wavelength perturbations necessary to confine high-energy CRs at the shock front. In particular Reville & Bell (2013) developed a formalism based on a spherical harmonic expansion of the Vlasov–Fokker–Planck equation that allowed them to investigate 3D configurations. The authors confirmed 2D linear results obtained in Reville & Bell (2012) and found a kind of universal behaviour of the shock precursor: oblique and perpendicular shocks behave very similarly to parallel shocks nearby the shock front where the magnetic field is found completely disordered. Caprioli & Spitkovsky (2013) also investigated CR-driven filamentation instabilities in a parallel shock configuration but using a dihybrid (hereafter termed as hybrid) method where electrons are treated as a fluid and protons as kinetic particles. Their 2D and 3D results confirmed the conclusions raised by Reville & Bell (2012) and show strong magnetic field amplification by NRS instability and further on by filamentation that lead to particle acceleration. Bai et al. (2015) have complemented the latter study by simulating parallel shock acceleration for configurations that prevail in young SNR using a PIC–MHD method. The authors have found a fast growth of magnetic field fluctuations in agreement with the linear analysis proposed in Bell (2004). They found that, in the precursor structure, cavitation and filamentation progress over time to larger sizes. They also found evidence of particle acceleration as result of multiple shock crossings. Hybrid simulations have also been performed in the oblique shock configuration by Caprioli & Spitkovsky (2014a) using 2D hybrid simulations. They reported on the drop of acceleration efficiency (defined as the number of particle reaching energies larger than 10 times the injection energy) and magnetic field amplification for oblique shocks with angles between the background magnetic field and the shock normal larger than $\sim 50^{\circ}$. This result is in apparent conflict with the results derived by Reville & Bell (2013). This issue is addressed in the present study.

In this study we consider the case of non-relativistic shocks corresponding with physical conditions that prevail in SNRs. We investigate several set-ups: parallel and oblique magnetic field configurations, different values of shock velocity and shock Alfvénic Mach numbers corresponding to different medium magnetization. Our simulations include the whole system including the shock front, whereas Reville & Bell (2012, 2013) only included a CR precursor in their analysis. We select the PIC–MHD method that allows us to study large space and time-scales of the shock problem, whereas the scales included in Caprioli & Spitkovsky (2013) were limited due to the hybrid approach. Finally, we generalize the solutions obtained by Bai et al. (2015) as our analysis is not restricted to parallel shocks while displaying for the first time the coupling between an adaptive mesh refinement (AMR) MHD description to a PIC approach of suprathermal particle dynamics. AMR grid is likely to become a key element of forthcoming numerical simulations if one hopes to describe CR acceleration and transport on the scale of actual astrophysical objects.

The paper lay-out is as follows:

(i) Section 2 describes the physical model that forms the basis of our treatment of the combined MHD and particle physics and a description of our numerical framework;

(ii) Sections 3 and 4 show the results of particle in MHD cells simulations (hereafter PI[MHD]C) dealing with parallel and oblique magnetic field amplification and particle acceleration occurring in the vicinity of non-relativistic astrophysical shocks;

(iii) Section 5 discusses of our results with respect to previous studies;

(iv) Section 6 delivers our conclusions regarding the use of AMR MHD coupled to PIC in order to describe the interplay between the magnetic field, the thermal plasma and the suprathermal particles.

2 THE PI[MHD]C FRAMEWORK

2.1 Physical context

Over the course of the last half-century, several methods have been developed to produce numerical simulations of the processes involved in the interaction between gas and magnetic field. Two of the most commonly used methods are grid-based MHD and PIC. Whereas the former deals primarily with large-scale structures, at the expense of the microphysics involved in the interactions, the latter focuses exclusively on the microphysics. Unfortunately, a large gap in scales exists in between these two regimes, where occur relevant astrophysical interactions for the problem of relativistic particle acceleration that are too large to be modelled effectively using the PIC method, and yet require the microphysics that MHD cannot provide. In this study we use a method that aims at combining these two approaches. This method will henceforth be referred to as particles in MHD cells: PI[MHD]C.

2.2 Grid-based MHD versus particle-in-cell

Grid-based MHD is a tried and proven method for simulating large-scale structures of gas interactions in a magnetic field. Grid-based MHD codes typically solve the equations of continuity and conservation of momentum, as well as an equation that describes the evolution of the energy (which can be conservation of total energy, but other options exist). Grid-based MHD is an efficient method that allows to quickly solve large-scale problems. Unfortunately, it only deals with statistical properties and does not include particle-based effects.

Unlike grid-based MHD, the PIC approach to gas dynamics treats the gas as a large collection of particles. This allows the user to describe physical effects that are based on the behaviour of individual particles, something that is not possible in grid-based MHD. The downside of the PIC approach is that it is numerically expensive, has a high level of numerical noise and hence can only deal with relatively small physical volumes and/or short physical time-scales. Both approaches however share common features as the fact that both have to provide a temporal description of the electromagnetic field occurring within the plasma. PIC codes usually use a Yee-type algorithm to solve the Maxwell equations, while MHD code solve the magnetic induction equation. In the non-relativistic MHD limit, it is generally assumed that the inertia of the thermal electrons can be neglected leading to a so-called Ohm's law linking the electric field to the magnetic field so that only magnetic terms enter the various MHD equations. In the context of astrophysical shocks where suprathermal particles carry electrical charges, such relationship between electric and magnetic field has to be revisited.

2.3 Combining both methods using Ohm's law

The large-scale description of particle acceleration occurring near astrophysical shocks stands as a challenge for PIC codes as such numerical method is inherently computationally expensive if one

considers large volume of gas. In many practical applications the majority of the particles behave as a thermal fluid and is described far more efficiently by grid-based MHD. It is only the (relatively) small number of non-thermal particles that need to be treated individually. Therefore, the key to handle simultaneously both the thermal fluid and the suprathermal particles is to achieve a mutual feedback in order to provide a self-consistent description of the interplay between both populations. Such link lies in the electromagnetic field whose interaction with both types of particles is the cornerstone of collisionless plasmas. In the context of non-relativistic MHD, the electric field can be expressed as a function of the magnetic field and the fluid velocity via a so-called Ohm's law. The presence of suprathermal particles within the thermal plasma leads to the addition of extra terms within the Ohm's law taking into account the electrical current and charge carried by these particles. Such an approach has been presented by Bai et al. (2015) considering a single particle species with a positive electrical charge. In the next subsection we generalized the aforementioned approach to any type of suprathermal particles (electrons and ions).

2.3.1 PI[MHD]C equations

The MHD conservation equations for mass, momentum and energy, including the additional terms that arise from the interaction with the non-thermal particles are

$$\frac{\partial \rho}{\partial t} + \nabla \cdot (\rho \, \boldsymbol{v}) = 0, \tag{1}$$

where ρ and $\boldsymbol{v}$ stand as the mass density and velocity of the thermal plasma,

$$\frac{\partial \rho \, \boldsymbol{v}}{\partial t} + \nabla \cdot \left(\rho \, \boldsymbol{v} \otimes \boldsymbol{v} - \frac{\boldsymbol{B} \otimes \boldsymbol{B}}{4\pi} + P_{\rm tot} \mathbb{I} \right) = - \boldsymbol{F}_{\rm part}, \tag{2}$$

with $\boldsymbol{B}$ being the magnetic field, while $P_{\rm tot} = P + B^2/8\pi$ is the total pressure. The energy equation reads

$$\frac{\partial e}{\partial t} + \nabla \cdot \left((e + P_{\rm tot}) \, \boldsymbol{v} + (\boldsymbol{E} - \boldsymbol{E}_0) \times \frac{\boldsymbol{B}}{4\pi} \right) = - \boldsymbol{u}_{\rm part} \cdot \boldsymbol{F}_{\rm part}, \tag{3}$$

where e is the total energy density of the thermal plasma. The new terms appearing on the right-hand side (rhs) of equations (2) and (3) involve an averaged suprathermal particle velocity $\boldsymbol{u}_{\rm part}$ and the opposite of the force density applied by the thermal plasma upon the suprathermal particle $\boldsymbol{F}_{\rm part}$. The definition of $\boldsymbol{u}_{\rm part}$ stems from the generalized Ohm's law expression, namely

$$c \, \boldsymbol{E} = -c \frac{\nabla P_{\rm e}}{n_{\rm e} e} + \left(\boldsymbol{J}_{\rm tot} - n_{\rm i} e \, \boldsymbol{v} - \sum_{\alpha} n_\alpha q_\alpha \boldsymbol{u}_\alpha \right) \times \frac{\boldsymbol{B}}{n_{\rm e} e}, \tag{4}$$

where $n_{\rm e}$ is the number density of thermal electrons, $n_{\rm i}$ is the number density of thermal ions. n_α is the average number density of suprathermal particle species α, q_α being its individual electrical charge, while $\boldsymbol{u}_\alpha$ stands for its average velocity. e is the positive elementary charge. We note the total non-thermal density as $n_{\rm part} = \sum_\alpha n_\alpha q_\alpha / e$. From charge conservation we have $n_{\rm e} = n_{\rm i} + n_{\rm part}$. As discussed by Bai et al. (2015), the terms related to the electron thermal pressure and the Hall current can be safely discarded provided we consider plasmas where the magnetic field pressure is not very small compared to thermal pressure and typical variation length scales larger than the ion skin depth. Considering the local electrical neutrality of the plasma and suprathermal population altogether, we obtain the expression of Ohm's law, namely

$$c \, \boldsymbol{E} = - \left((1 - R) \, \boldsymbol{v} + R \, \boldsymbol{u}_{\rm part} \right) \times \boldsymbol{B}, \tag{5}$$

where $R = \sum_\alpha n_\alpha q_\alpha / n_{\rm e} e$ is a direct measure of the relative density of suprathermal particles. The average velocity of the whole suprathermal population is

$$\boldsymbol{u}_{\rm part} = \frac{\sum_\alpha n_\alpha q_\alpha \boldsymbol{u}_\alpha}{\sum_\alpha n_\alpha q_\alpha} = \frac{\boldsymbol{J}_{\rm part}}{n_{\rm part} e}. \tag{6}$$

Additionally we define

$$\boldsymbol{E}_0 = - \frac{\boldsymbol{v}}{c} \times \boldsymbol{B} \tag{7}$$

as the electric field that would be generated by the thermal gas alone. The actual electric field, $\boldsymbol{E}$, generated by both thermal and non-thermal populations combined is related to the force applied by the thermal gas upon suprathermal particles, namely

$$\frac{\boldsymbol{F}_{\rm part}}{n_{\rm i} e} = (1 - R) (\boldsymbol{E}_0 - \boldsymbol{E}). \tag{8}$$

The Lorentz force $\boldsymbol{F}_{\rm part}$ can be expressed as

$$\boldsymbol{F}_{\rm part} = (1 - R) \left(n_{\rm part} e \boldsymbol{E}_0 + \frac{\boldsymbol{J}_{\rm part}}{c} \times \boldsymbol{B} \right). \tag{9}$$

In order to close the set of PI[MHD]C equations, we consider the temporal evolution of the magnetic field provided by the Maxwell–Ampere equation,

$$\frac{\partial \boldsymbol{B}}{\partial t} = c \nabla \times \boldsymbol{E}. \tag{10}$$

For the sake of completeness we have to consider the total electric field generated by both populations in the induction equation.

2.3.2 Particle motion

Most of the astrophysical shocks involve collisionless plasmas where one can safely discard collisions between particles. The equation governing the motion of individual suprathermal particles will then only take into account the electromagnetic force, namely

$$\frac{\partial \boldsymbol{p}_{\alpha,j}}{\partial t} = q_j \left(\boldsymbol{E} + \frac{\boldsymbol{u}_{\alpha,j}}{c} \times \boldsymbol{B} \right), \tag{11}$$

with $\boldsymbol{p}_{\alpha,j}$, q_j and $\boldsymbol{u}_{\alpha,j}$ the momentum, charge and velocity of particle j. Inserting equation (5) for the electric field leads to the following equation:

$$\frac{\partial \boldsymbol{p}_{\alpha,j}}{\partial t} = \frac{q_\alpha}{c} \left(\boldsymbol{u}_{\alpha,j} - (1 - R) \, \boldsymbol{v} - R \, \boldsymbol{u}_{\rm part} \right) \times \boldsymbol{B}, \tag{12}$$

where we see that contributions from the thermal plasma and the average velocity of suprathermal particle do influence the motion of a single particle. Within a given MHD cell, one can express the energy balance regarding all suprathermal particles located in this cell as

$$\sum_\alpha \sum_j n_\alpha \boldsymbol{u}_{\alpha,j} \cdot \frac{\partial \boldsymbol{p}_{\alpha,j}}{\partial t} = \boldsymbol{u}_{\rm part} \cdot \boldsymbol{F}_{\rm part}, \tag{13}$$

which shows that the total energy is conserved as the suprathermal population exchanges energy with the thermal plasma and magnetic field.

2.4 Numerical approach

We use the MPI-AMRVAC (van der Holst, Keppens & Meliani 2008) code as a basis. This is a fully conservative, finite-volume code that solves conservation equations on an adaptive mesh grid and uses

the OpenMPI library for running in parallel on systems with distributed memory architecture. In order to create a high-performance PI[MHD]C code, we maintain the existing architecture of the code but replace the standard equations of ideal MHD with equations (1)–(3). We have also created an additional module that includes the additional physics required to deal with PIC treatment of individual particles.

The MPI-AMRVAC code is fully 3D, but for the study presented in this paper, we limit ourselves to 2D3V applications, namely using a 2D spatial grid while velocity and electromagnetic field exhibit three components. In the following paragraphs we present the various new features added to the MPI-AMRVAC code.

2.4.1 *PI[MHD]C code structure*

Finite volume MHD codes rely on a grid of given geometry where MHD quantities are defined at the centre of each cell of the grid. In order to compute the MHD fluxes occurring through each cell interface, one needs to accurately approach the solution of the corresponding Riemann problem using a given MHD solver combined to a slope limiter. On the other hand, PIC codes usually define physical quantities at different locations on the grid when they employ a Yee-type algorithm. For instance, magnetic fields are defined at the centre of the cells, while electric fields and current density are set on the cell edges and charge density at the corners.

In order to couple both approaches with the minimum amount of numerical computations, we choose to use the MHD grid as a base and to consider an offset PIC grid where MHD cell centres stand as PIC cell corners. Such choice allows us to simply map the charge and current densities generated by the particles on to the MHD grid without any interpolation procedure. Mapping the charge and current densities is achieved through standard second-order cloud-in-cell techniques (Ferrell & Bertschinger 1994).

The temporal evolution of the simulation follows the following pattern. At the beginning of each time step, the MHD quantities are saved. We then advance them for one MHD time step according to the equations derived in Section 2.3, which include both the magnetohydrodynamical properties of the thermal gas and the charge and current generated by the non-thermal particles. We then evolve the particle positions and velocities of the suprathermal particles using a relativistic form of the Boris method (Birdsall & Langdon 1991, and references therein) based on the MHD quantities from the beginning of the MHD time step. Finally, we map the charge and current densities, as determined by the new particle distribution in phase space, on to the grid. At this point the time step ends and the process repeats itself. It is noteworthy that MHD time step [based on Courant–Friedrich–Levy (CFL) condition] and PIC time step (imposed by particle dynamics) do not match. As PIC time step is usually smaller than the MHD ones, we have the possibility to perform several PIC time steps within one given MHD step. However, in order to maintain the simulation coherence, we do not allow more than a few PIC steps within one MHD step (see Bai et al. 2015).

2.4.2 *Adaptive mesh refinement*

The MPI-AMRVAC code uses the Octree system of AMR (Shephard & Georges 1991). This system divides the physical domain of the simulation into a number of identical grids, which can be independently refined. Each time a grid is refined, it is subdivided into 2^D similar grids that are D-dimensional. The decision on whether or not to refine is based on the variance of one or more selected variables within a grid. If the variance exceeds a pre-set limit, then the grid is refined. Conversely, if the variance gets below a given limit within a part of the computational domain, then the grid is coarsened. The Octree system further ensures that adjacent grids never differ by more than one level of refinement. Implementing PI[MHD]C, we maintain this structure, but put in an additional condition: if the number of particles within a grid reaches 25 per cent of a pre-set maximum, the grid is no longer allowed to coarsen. If the number of particles reaches 80 per cent of the maximum, the grid is refined (assuming it has not yet reached the maximum refinement allowed). Additionally, the grid can be set to refine if the average Larmor radius of the particles within the grid becomes smaller than a pre-set number times the size of the individual grid cells. This ensures that the Larmor radius is always resolved (see also Section 2.4.4).

At the boundaries between grids, each grid has a set of 'ghost cells', which provide it with information from its neighbours. For usual MHD without AMR the values in these ghost cells are a simple matter of copying the values from the neighbour. In case AMR is triggered, then one must rely on coarsening/interpolating procedures to provide the necessary data from coarser/finer neighbouring grids. However, PIC-related variables (charge and current density) are a different matter. Because each particle contributes to the surrounding grid cells, a charged particle lying near the boundary will also contribute to the ghost cells and its contribution must be preserved. So, rather than overwriting the contents of the ghost cells with values from neighbouring grids, these values have to be added up. Similarly, the original values of the neighbour ghost cells have to be added to the grid cells inside the boundary. This discrepancy between MHD and PIC approaches requires a specific boundary treatment regarding the different quantities while preserving computational efficiency.

A particular problem that has to be considered when combining PIC treatment with an adaptive mesh is how to deal with particles that move from a coarser grid to a finer one, or the other way round. The area of influence of a particle is determined by the size of the mesh, not the physical domain. As a result, when a particle moves from a coarse to a fine grid, its area of influence is reduced. To compensate for this, and conserve charge and current, the effective weight of the particle has to be increased by a factor equivalent to the reduction in effective volume. An alternative method would be to split particles when they enter a more refined grid. However, this would cause additional problems: the number of particles would increase rapidly, negating part of the advantage of the PI[MHD]C method. It would also require additional treatment when the particles returned to a coarser grid: either we would have to recombine particles (not a practical approach because there is no guarantee that the correct number of particles would leave the more refined area at the same time), or we would have to accept that we would have multiple particle species in each grid, with their charge and mass determined by whether or not a particle had passed through a highly refined area at any given time during the simulation. In order to avoid these issues, we do not split particles, but instead scale its effective weight to conserve the charge.

Another concern, when incorporating AMR and PIC in the same code, is the treatment of boundaries between grids with different levels of resolution. Because the area of influence of each particle is determined by the mesh size, rather than a physical domain, the boundaries require careful treatment in order to ensure that charge and current density are conserved across the grid boundaries. We achieve this by keeping the physical size of the stencil for particles in the grid with the coarser mesh the same, which means that it gets spread over two rows of grid cells in the more refined grid

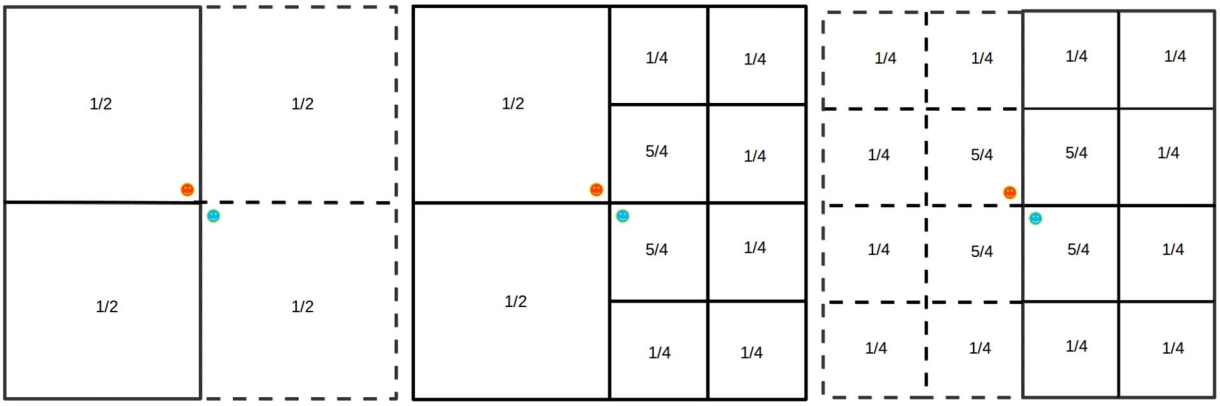

Figure 1. Distribution of particle weights at the edge of two grids with different levels of refinement. Two particles are sitting close together near the intersection. One (red) just inside the coarser grid, the second (blue) just inside the finer grid. Continuous lines show the actual domain, the dashed lines are ghost cells. The left-hand side figure shows how it is perceived by the coarser grid, the right-hand side figure shows how it is perceived by the finer grid. In both cases, the charge distribution is symmetrical around the two particles. The figure at the centre shows the actual charge density as seen in the output.

(see Fig. 1). This method guarantees that the charge distribution is symmetrical around the particle, both according to the coarser and the finer grid, even though it seems asymmetric in the output.

2.4.3 *Maintaining a divergence-free magnetic field*

A potential downside of the finite-volume approach is that it does not guarantee that the magnetic field remains divergence free. This is of particular concern when using the PI[MHD]C method, especially in situations where the number of particles in a given area is low. In order to solve this potential problem we have implemented within the MPI-AMRVAC code a constrained-transport algorithm based on Balsara & Spicer (1999). In such approach, numerical fluxes provided by the MHD solver (which also include terms from suprathermal particles) are used to enforce the solenoid nature of the magnetic field.

2.4.4 *Resolution and time step control*

The initial MHD grid resolution is determined by the user and the number of refinement levels allowed in the simulation. Such choice must be done carefully since MHD and PIC methods use fundamentally different criteria to determine the correct resolution. For grid-based MHD the primary consideration for the size of individual grid cells is that they should be smaller than the size of the structures that occur in the simulation, in order to ensure that the morphology of the gas is fully resolved. It is important to recall here that validity of the MHD description imposes that the size of the phenomenon occurring in the simulation has to remain larger than ion skin depth $c/\omega_{\mathrm{p,i}}$ where $\omega_{\mathrm{p,i}}^2 = 4\pi n_{\mathrm{i}} e^2/m_{\mathrm{i}}$. In order to enforce that condition, we then make sure that the size of cell embedded in the most refined level of the AMR is larger than the local ion skin depth.

Regarding PIC simulation the required resolution depends on the Larmor radius of the particles, which needs to be well resolved to ensure that the code captures the particle trajectories properly. For PI[MHD]C simulations the users will have to determine on a case-by-case basis which effects they have to resolve and adjust the resolution accordingly. For example, it is perfectly possible to utilize the code without resolving the Larmor radius. However, this will cause the effect of the particles on the MHD quantities to be reduced. Since the influence of each particle is spread over multiple grid cells, the effect of the small motions of a particle within a single cell tends to become diffusive. If the Larmor radius is not resolved, the gyrating motion of the particles around the magnetic field lines can be effectively lost. In order to avoid this issue we have added a refinement criterion over particle Larmor radius to the mesh refinement conditions. If the average Larmor radius of the particles within a grid falls below a pre-set fraction of the cell size, the grid is refined.

In an explicit MHD code, time step size and resolution are linked through the CFL condition:

$$\Delta t \leq C \min\left(\frac{\Delta x}{v_{\mathrm{max}}}\right), \tag{14}$$

with Δt the time step, C a constant (usually less than 1), Δx the size of a grid cell and v_{max} the maximum speed at which a signal travels through the gas. The latter is calculated as the sum of the bulk motion of the thermal fluid and wave velocities, such as sound and Alfvén speed. A similar condition applies to the PIC part of the code, but with v_{max} being the maximum speed of an individual particle.

Since particles will typically travel much faster than the thermal plasma, it is usually the PIC part of the code that limits the amplitude of the time step. In order to increase computational efficiency, we allow for the possibility to let the code take multiple PIC steps within a single MHD time step. When this is done, the magnetic and electric fields are kept frozen for the duration of several PIC time steps, until the code has reached the next MHD time step. Obviously, this method must be used with care, but it decreases the computation time and can be applied safely for situations where the gas only responds slowly to non-thermal particles.

An additional check is placed on the time step. This becomes important if particles have a gyroradius that is smaller than the size of a single grid cell, which is possible once the grid has reached the maximum level of refinement. At this stage the CFL condition no longer guarantees that the motion of the particle is properly resolved. Therefore, we also limit the time step to a certain fraction of the gyrotime.

3 PARTICLE ACCELERATION AT NON-RELATIVISTIC SHOCKS: PARALLEL MAGNETIC FIELD CASE

In order to test our newly developed AMR-PI[MHD]C code, we first consider a new set-up to study the interaction between a single suprathermal particles species (protons) and a plane shock with the magnetic field perfectly aligned with the direction of propagation of the shock. A similar simulation has been presented in Bai et al. (2015) where the authors have explored the impact of particle injection upon magnetic field amplification and particle acceleration at collisionless astrophysical shocks. If the physical conditions are similar to the simulation presented in Bai et al. (2015), our simulation is performed in the shock frame rather than in the upstream fluid frame. Such a choice enables us to follow the evolution of the shock more easily.

3.1 Simulation set-up

The simulation is run in a box with a size of 240 × 30 times a reference Larmor radius $r_g = v_{inj}/\omega_c$, corresponding to the gyroradius of particles injected with a velocity v_{inj} propagating in the upstream magnetic field with a ion-cyclotron pulsation $\omega_c = q/mcB_0$ The base level of the grid contains 240 × 30 grid cells. We allow the adaptive process to use three mesh levels of refinement depending on the MHD physical conditions throughout the domain. Additionally one extra level of refinement can be used in case the number of particles located in one grid approaches a maximum limit set to 7×10^4. Enabling an extra level of refinement prevent losing particles while maintaining the computational efficiency. As a result, our grid can reach a maximum effective resolution of 3840 × 480 cells. We chose to use a TVDLF solver, combined with a van Leer flux limiter. Such a combination leads to a robust but precise numerical scheme able to capture the small-scale features of the plasma and magnetic field.

At the start of the simulation we set up a shock following the Rankine–Hugoniot conditions with an upstream velocity of $V_{sh} = 3 \times 10^{-3}c$ along the x-axis, flowing from the right x-boundary towards the left x-boundary. In order to recover an Alfvénic Mach number of $M_A = 30$, we set the Alfvén speed to $V_{A0} = 10^{-4}c$. We also assume that in the upstream medium magnetic and thermal energies are in equipartition (i.e. ($E_B = E_T$)). Following Bai et al. (2015) we inject suprathermal particles in the downstream medium close to the shock front with an isotropic velocity $v_{inj} = 3V_{sh}$ in the downstream fluid frame. The number of particles injected at every time step is determined so that the mass ratio of the injected particle to the thermal plasma mass flux is 2×10^{-3}.

We choose inflow and outflow conditions at the right and left x-boundaries, respectively, to accommodate the flow of the thermal plasma. For the non-thermal particles we assume that any particle that reaches the x-boundaries escapes from the system. For the y-axis, we use periodic boundary conditions for both the thermal gas and the non-thermal particles.

To ease comparison, all times are expressed in ω_c^{-1} unit. Axis length scales are measured in gyroradii units r_g. It is noteworthy that this fiducial length can be related to the ion plasma skin depth, namely $r_g = cv_{inj}/V_{A0}\omega_{p,i} = 90c/\omega_{p,i}$ in the upstream medium. This shows that any grid belonging to the highest refinement level have MHD cells whose size is at least five times the local ion skin depth. It hence ensures that our MHD description remains valid everywhere. Finally particles are injected at a constant rate at the shock, such that 2×10^7 particles are injected over a simulation time of $2 \times 10^3\omega_c^{-1}$.

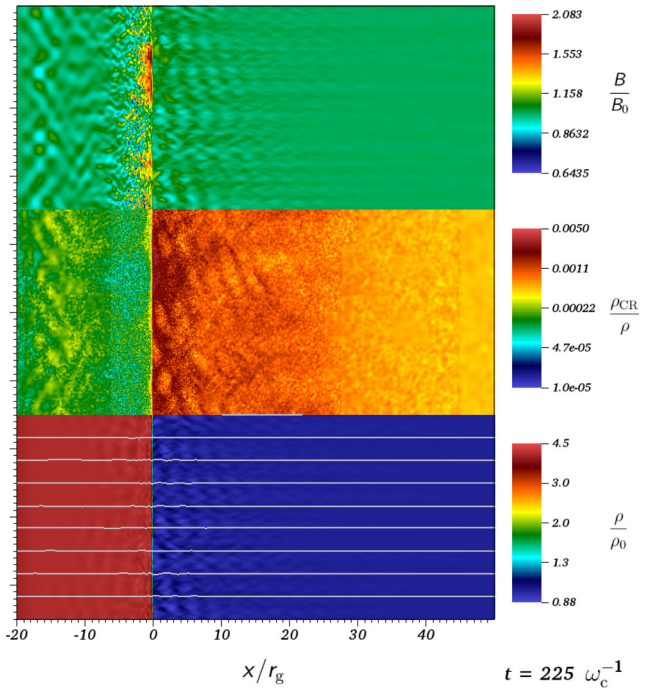

Figure 2. Colourmaps of the magnetic field amplitude, CR density and plasma density in the early stages of the parallel shock simulation ($\theta_B = 0$, $M_A = V_{sh}/V_{A0} = 30$). This figure shows, from top to bottom, magnetic field strength relative to the original magnetic field, non-thermal particle charge density relative to the thermal gas density and thermal gas mass density relative to the upstream density at the start of the simulation, combined with the magnetic field stream lines. The gas is streaming through the shock from right to left. At this point in time ($t = 225\omega_c^{-1}$) the upstream medium shows the start of the streaming instability, while the downstream medium shows the onset of turbulence. Axis are normalized to r_g, namely the gyroradius of injected particles in the upstream medium.

3.2 Results

From the start, the effect of charged particles on the magnetic field varies considerably between upstream and downstream regions as shown in Fig. 2, which shows at time $t = 225\omega_c^{-1}$: the gas density relative to the initial upstream density ρ_0, the particle density relative to the gas density and the absolute magnetic field strength relative to the initial upstream magnetic field B_0.

As particles move upstream, they spiral around the field lines, initiating the NRS instability (Bell 2004), which is characterized by a filamentary structure that runs parallel to the field lines and the flow. Because the bulk motion of the gas is super-Alfvénic, the motion of the thermal plasma dominates over the fluctuations in the magnetic field, keeping the instabilities aligned with the flow. On the other hand, the effect in the downstream region is much more complex. Although the downstream flow is not sub-Alfvénic, the difference between bulk velocity and Alfvén speed is much reduced by the shock, allowing the magnetic fluctuations to start moving perpendicular to the flow. As a result, the fluctuations look random, both in strength and direction. They neither follow the field lines nor the flow. The strongest magnetic fluctuations occur downstream, just behind the shock. Here the effect of the upstream and downstream instabilities is combined, with the upstream instability being enhanced as it is compressed by the shock. One way to clearly identify this instability process is to compute the power spectrum of magnetic field fluctuations transverse to the mean magnetic field. Indeed, as predicted by the linear theory of the instability, the fastest

growing mode of the instability is controlled by the strength of the suprathermal particle current as $k_{\max} = J_{\rm CR}/2B_0$. The upper panels of Fig. 6 shows at $t = 225\omega_{\rm c}^{-1}$ the transverse power spectrum and the particle current. It clearly appears that upstream the power spectrum peaks at the expected wavenumber, namely $k_{\max} \simeq 0.02\omega_{\rm pi}/c$. The transverse power spectrum is defines as

$$S_{\perp}(k) = \frac{|\delta \hat{B}_{\perp}^2(k)|}{B_0^2}, \tag{15}$$

where k is the wave vector oriented along the mean magnetic field B_0 and $\delta \hat{B}_{\perp}(k)$ stands for the Fourier transform of the transverse magnetic field. The downstream counterpart of the spectrum exhibits the same behaviour but with a dominant mode roughly four times larger than that for the upstream spectrum. This behaviour is consistent with Alfvén waves wave vector transmission at a parallel non-relativistic shock (Vainio & Schlickeiser 1998). In Fig. 6, the magnetic power associated with transverse magnetic fluctuations remains small compared to the mean magnetic field energy density, a clear sign that the instability is still in a linear growth phase.

As a result of these two different patterns, the motion of the particles changes as well. Upstream the particles can effectively escape from the domain by moving upstream, along the field lines, until they hit the boundary. However, because the downstream magnetic field acquires significant y- and z-components, the particles that move downstream are delayed as their motion is twisted to follow the local magnetic field, hence experiencing a random walk. As a consequence, the turbulent zone effectively becomes a barrier that few particles are able to pass. Instead, they are either reflected into the upstream medium, or become trapped inside the turbulent zone downstream. Conversely, owing to the parallel filamentary nature of the instabilities upstream, the particles that move upstream do not encounter an effective magnetic barrier and can escape quite easily. However, we should note that the particle confinement is influenced by the 2D nature of our simulations as the non-linear growth of the instability may differ from full 3D computations (see Bell et al. 2013 where authors considered both 2D and 3D Vlasov–MHD simulations).

When the instabilities increase in strength, the thermal plasma starts to respond, following the local motion of the magnetic field. Upstream, this leads to an enhanced filamentary structure, whereas downstream the medium becomes increasingly turbulent. This turbulent zone effectively traps the non-thermal particles, increasing their local density, which in turn increases the instability (Fig. 3). Meanwhile, the amplification of the magnetic field rises until, locally, it reaches values of approximately 15 times the original strength. It is noteworthy that the transverse magnetic power spectrum in the late phase of the simulation still exhibits dominant modes in agreement with the NRS instability in the precursor, while downstream fluctuations have increased well beyond the initial magnetic field strength and are spread over a large range of wave vectors. This last feature is of great interest for particle acceleration as it is mandatory to create large-scale magnetic fluctuations in order to induce a random motion of more and more energetic suprathermal particles (Zirakashvili et al. 2008).

At later times, the particle current starts to influence the shock itself, which starts to move as it adjusts to local variations in density, velocity and pressure. Eventually, the shock becomes warped to the point that it becomes impossible to define its exact location (Fig. 4). At this moment we stop the simulation because we are not able to inject particles at the shock front anymore because the injection process becomes dependent of the shock structure itself. Longer term simulations require a more careful analysis of the injection procedure and are scheduled for a future work.

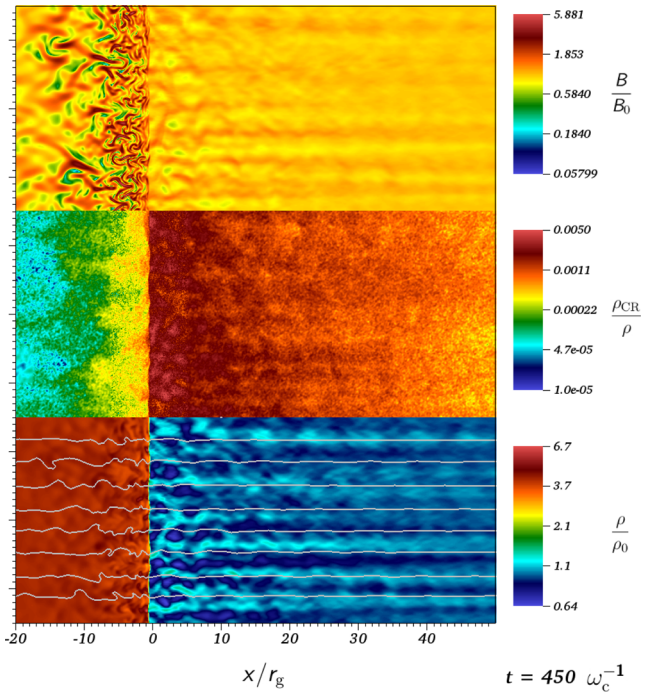

Figure 3. Similar to Fig. 2, but it shows the conditions at $t = 450\omega_{\rm c}^{-1}$. Both the upstream streaming instability and the downstream turbulence are now fully developed.

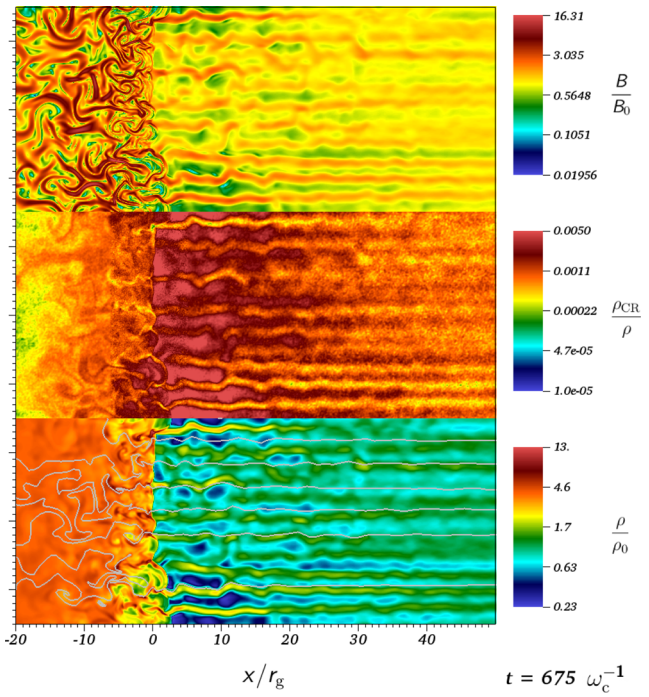

Figure 4. Similar to Figs 2 and 3, but it shows the conditions at $t = 675\omega_{\rm c}^{-1}$. The shock is warping in response to the instabilities.

Fig. 5 shows the energy spectra of suprathermal particles contained within the computational domain at different stages of the simulation. In the early stages, the particle energy distribution remains peaked around the injection energy, while as the simulation

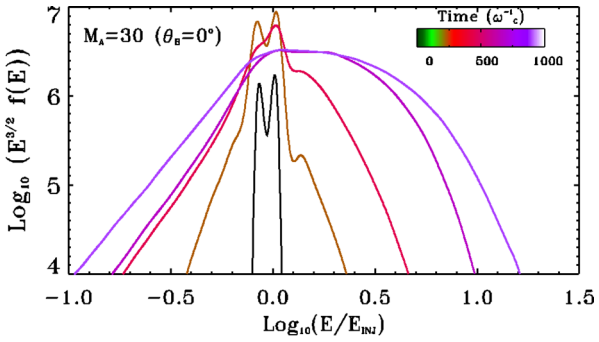

Figure 5. Energy spectra of non-thermal particles injected at energy $E_{\rm inj}/m_{\rm i}c^2 = 4 \times 10^{-5}$. The various spectra correspond to simulation displayed in Figs 2–4. A non-thermal tail is forming in the late stages of the simulation tending to a power-law spectrum in agreement with a diffusive shock acceleration process.

progresses particle distribution broadens. Beyond $t = 350\omega_{\rm c}^{-1}$ a high-energy tail appears and tends to form a power law whose index is in agreement with diffusive shock acceleration theory, namely $f(E) \propto E^{-3/2}$, where E is the kinetic energy of the particles. In our simulation, the tail formation stalls beyond $t = 600\omega_{\rm c}^{-1}$ mainly due to the deformation of the shock front leading to a deficient particle injection.

Finally, we have performed a simulation without any AMR refinement while setting all the computational domain to the most refined level. With such settings, we have basically recovered all the results from the previous simulation. In Fig. 6, we plot in dashed line the power spectrum of the transverse magnetic fluctuations obtained in the case where no AMR grid is triggered: the downstream magnetic spectrum is recovered and the same dominant mode of the turbulence is present in each phase of the simulation. Such a test proves that the use of an AMR grid is suitable to perform PI[MHD]C simulations and even recommended for future applications requiring a much larger computational domain.

3.3 Higher Mach number simulations

We repeat above simulations for an increased Alfvénic Mach number ($M_{\rm A} = 300$), which corresponds more closely to the type of shock expected of the early phase of a supernova remnant expansion into the interstellar medium (ISM). Higher Mach numbers are achieved by increasing the velocity of the thermal fluid by an order of magnitude. The initial velocity of newly injected particles is increased by the same amount. In order to keep the other quantities (density, magnetic field strength) identical, we also

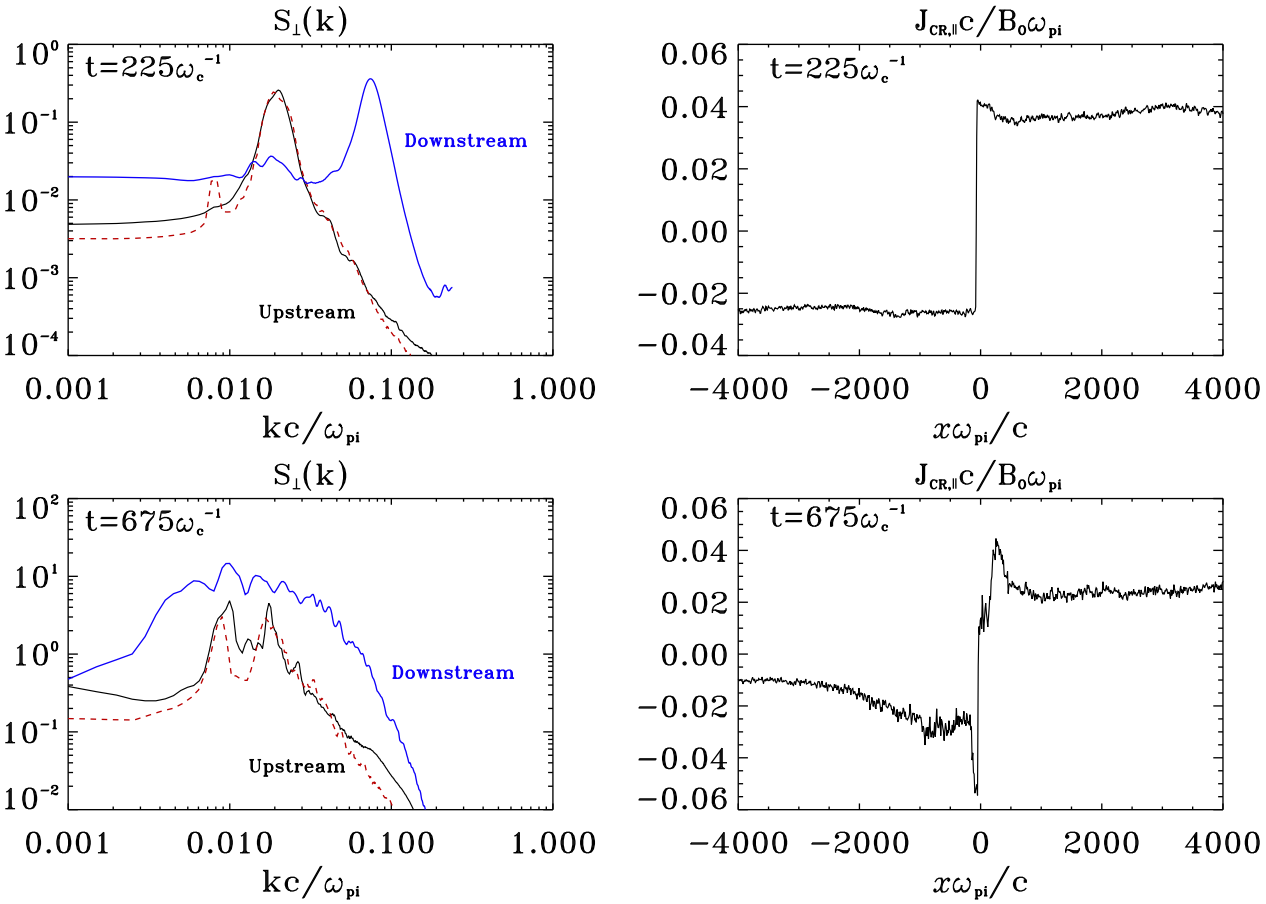

Figure 6. Transverse magnetic power spectrum and CR current along the mean magnetic field in both upstream and downstream media. Upper panels correspond to an early stage of the simulation corresponding to Fig. 2, while lower panels stand for a later stage corresponding to Fig. 4. Let us note that the red dashed line in both power spectrum plots corresponds to the upstream spectrum obtained by performing the same simulation but without any AMR refinement/coarsening, namely by setting the entire grid at the highest resolution. The relatively good agreement between upstream spectra shows that the use of AMR MHD is suitable to depict the CR/magnetic field/thermal plasma interaction.

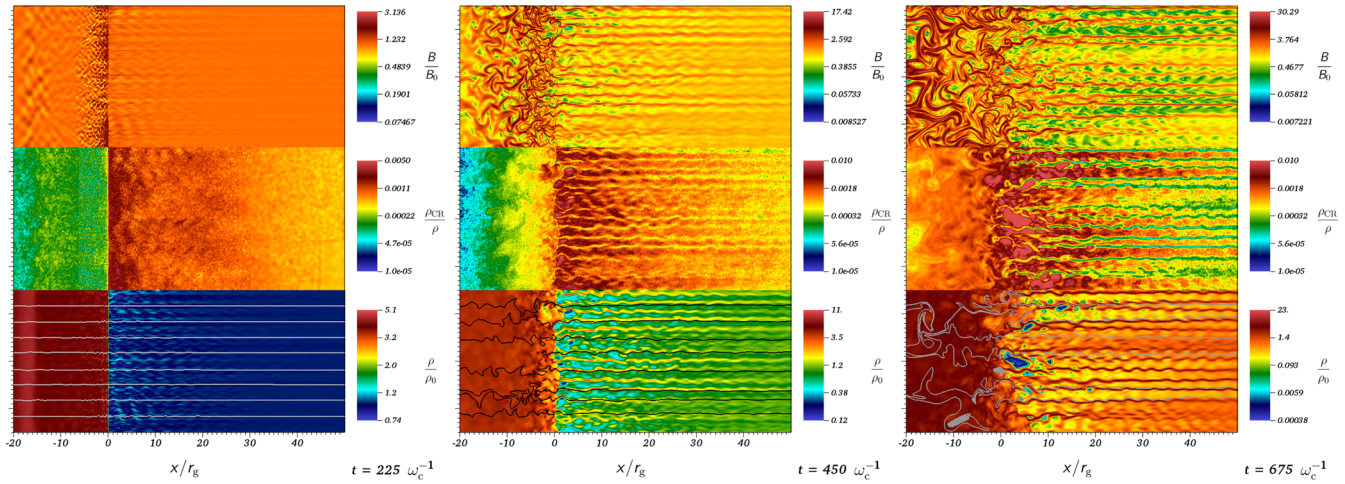

Figure 7. Same plots than in Fig. 2 showing the temporal evolution of a high Alfvénic Mach number shock ($\theta_B = 0$, $M_A = 300$). In all the stages of the simulation we recover the same patterns than in the slower shock simulation displayed in Figs 2–4. However, one difference arises, namely the amplification of the magnetic field. In this simulation, the average magnetic field in the downstream medium has been amplified by a factor of 3 with respect to slow shock case. This result is in relative good agreement with the pure kinetic simulations of Caprioli & Spitkovsky (2014a,b).

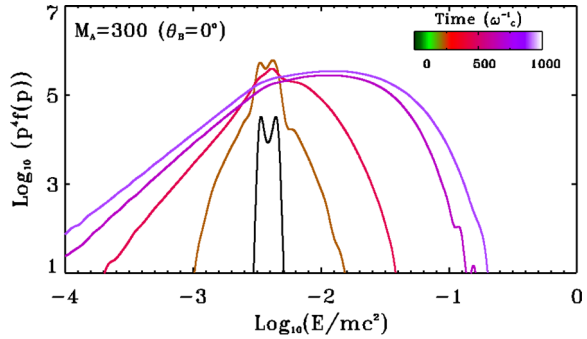

Figure 8. Energy spectra of non-thermal particles injected at energy $E_{inj}/mc^2 = 4 \times 10^{-3}$. The various spectra correspond to simulation displayed in Fig. 7.

increase the Larmor radius by a factor of 10 and increase the size of the simulation box accordingly, while maintaining the PIC resolution (the number of grid cells per Larmor radius). As shown in Figs 7 and 8, the behaviour of the shock follows the same pattern as for the $M_A = 30$ case, albeit that the local magnetic field amplification is approximately three times as strong. This last result is in agreement with the pure kinetic (hybrid PIC) computations presented by Caprioli & Spitkovsky (2014b) where the authors have investigated the role of the Alfvénic Mach number of the shock over the magnetic field amplification near a non-relativistic shock. We have considered here a $M_A = 300$ shock and found that the amplified magnetic field at saturation follows the same relation where $< B_{tot}^2/B_0^2 > \sim 0.45 M_A$. Such an agreement between full PIC simulation and PI[MHD]C computations highlights the viability of the latter method. It is important to mention that we have performed simulations of shocks exhibiting an Alfvénic Mach number up to $M_A = 3000$ thanks to the robustness of the PI[MHD]C method and again recover the basic same patterns than in the $M_A = 30$ case. In a forthcoming study we will explore the process of magnetic field amplification and particle acceleration in relativistic shocks.

4 PARTICLE ACCELERATION AT MAGNETICALLY OBLIQUE SHOCKS

In this section we consider the process of particle acceleration near oblique astrophysical shocks where a mean magnetic field is inclined at an angle θ_B with the propagation direction of the shock. Pure kinetic computations have considered such a configuration and have concluded that when $\theta_B > 45^\circ$, neither magnetic field amplification nor significant particle acceleration is taking place (see for instance Caprioli & Spitkovsky 2014a and reference therein). The goal of the simulations presented in this section is to put this statement to the test by investigating over a long period of time the interplay between suprathermal particles and an oblique super-Alfvénic MHD shock. To do so, we choose to consider a $\theta_B = 70^\circ$ oblique shock with various Alfvénic Mach numbers fulfilling the Rankine–Hugoniot jump conditions in the shock frame.

4.1 Moderate Alfvénic Mach case ($M_A = 30$)

The injection process of suprathermal particles follows the same recipe than in the parallel case, namely injecting particles with an isotropic velocity $v_{inj} = 3V_{Sh}$ in the downstream frame. Injection occurs close to the shock front in the downstream medium. As mentioned in previous studies (see e.g. Caprioli, Pop & Spitkovsky 2015, and references therein), injected particles reaching the shock can be reflected at the shock front because of the obliquity of the magnetic field. Return to the shock is then quite unlikely in the early phase of the magnetic field amplification as there are no significant magnetic fluctuations that can alter the trajectory of the particles. The various toy models presented in previous studies agree to state that shocks exhibiting oblique magnetic field verifying $\theta_B > 45^\circ$ are not allowing a sufficient amount of particle to get into the upstream medium to trigger NRS instability.

4.1.1 Initial shock drift acceleration

As we inject particles near the shock, we notice that in the very first stages of the simulation, the particle energy distribution function, originally peaked around injection energy, is now expanding rapidly

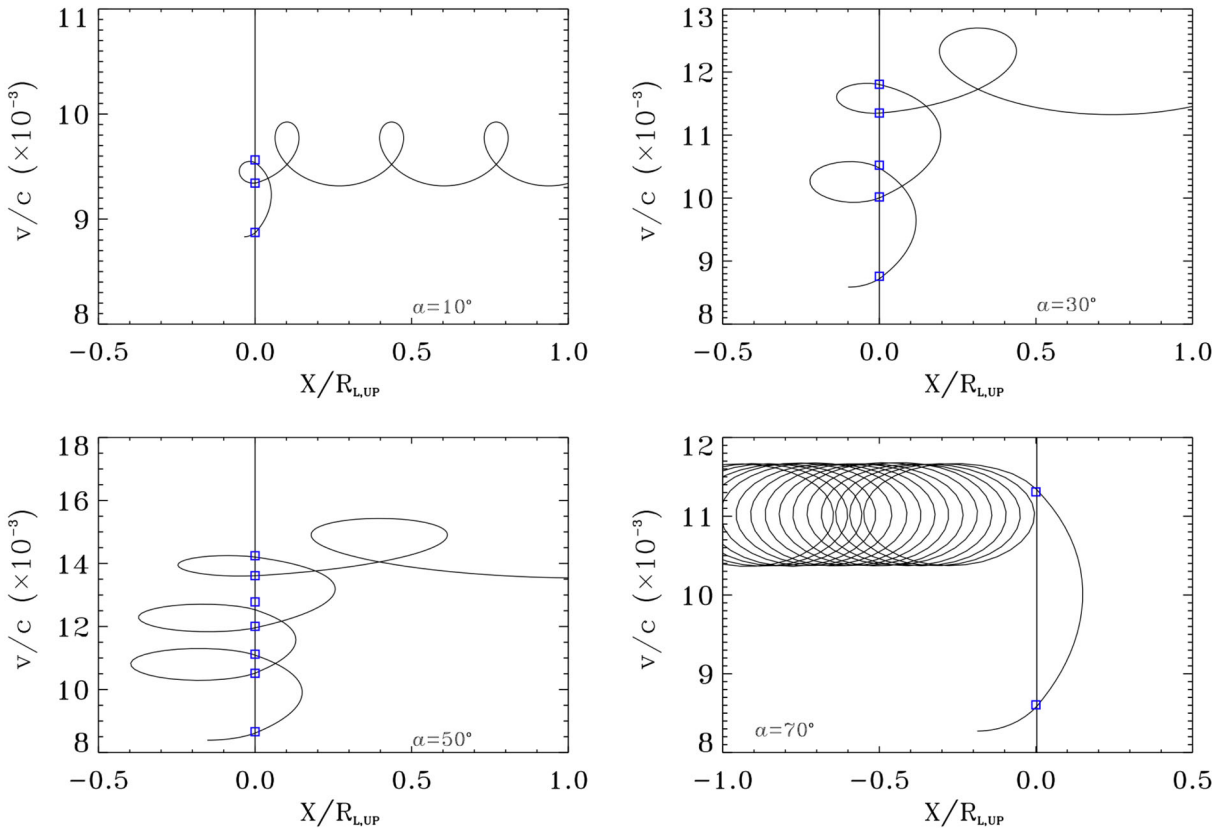

Figure 9. Evolution of the velocity of four suprathermal particles injected in the downstream medium with an initial velocity of $3V_{\rm sh}$ in the downstream frame. Each particle is injected with a different pitch angle α with respect to the oblique magnetic field ($\theta_B = 70^\circ$). Blue rectangles stand as energy gains predicted by the scattering of particle upon a thin shock when considering initial properties of the particles.

up to a point where the most energetic particles reaches 10 times the injection energy (see Fig. 14). This distribution function then stalls until approximately time $t = 200\omega_{\rm c}^{-1}$. We checked the path of many particles and found that the accelerated particles have experienced multiple shock encounters, while many particles have roughly kept their initial energy.

In Fig. 9, we have displayed the velocity variation as a function of the x coordinate of four particles, each one of them being injected with a different pitch angle α with respect the downstream magnetic field. Some of these particles experienced multiple shock crossings leading to a so-called shock drift acceleration process (SDA; see e.g. Decker 1988). Since numerical MHD schemes display shock discontinuities as a velocity transition occurring over a few MHD cells, one may question the ability of PI[MHD]C code to properly depict the particle acceleration process. In order to test the accuracy of the code, we have added on top of the particle trajectory in the x–v space in Fig. 9 the velocity jump gained by each particle going from downstream to upstream and then back to downstream. This estimate is straightforward as we record the velocity and pitch angle of the particle when crossing the shock and compute the velocity jump accordingly to the conservation of the particle velocity in the upstream frame, namely

$$\Delta v = \left(\left(v_{\rm o}'\mu_+ + U_{\rm u}\right)^2 + v_{\rm o}'^2\left(1-\mu_+^2\right)\right)^{1/2} - \left(\left(v_{\rm o}'\mu_- + U_{\rm u}\right)^2 + v_{\rm o}'^2\left(1-\mu_-^2\right)\right)^{1/2}, \quad (16)$$

where $v_{\rm o}'$ is the velocity of the particle when entering the upstream medium measured in the upstream frame, while μ_- and μ_+ are the cosine of the pitch angle of the particle when entering the upstream medium and going back to the downstream medium, respectively, $U_{\rm u}$ is the flow speed in the shock rest frame. The good agreement between the few x–v paths and the aforementioned prediction shows that the numerical MHD shock transition is narrow enough to accurately describe the particle acceleration via SDA. This is obviously achieved thanks to the numerical set-up of the simulation leading to the Larmor radius of the injected particle being larger than the MHD shock thickness.

As soon as we inject suprathermal particle behind the shock, they experienced SDA leading to a shift from the initial monoenergetic energy distribution to a wider energy distribution as one can see in Fig. 14. We do observe that particles either gain or lose energy depending on their injection orientation and that the highest velocity obtained through SDA is roughly three times the injection velocity, namely $9V_{\rm sh}$. Such process has already been observed in hybrid simulations (see e.g. Caprioli & Spitkovsky 2014a) but the use of PI[MHD]C techniques provides here an advantage as the pool of suprathermal particles in our simulations is far larger than in hybrid computations. Indeed, we do inject up to 20 million suprathermal particles in the span of the simulation. In order to reach such statistic, a hybrid simulation would have to consider roughly 20 billion particles crossing the shock. In our simulation, the most energetic particles are able to flow into the upstream medium as they are able to counteract the drift velocity induced by the presence of the electromotive field. As a result of the drift motion, the CR current is no longer parallel to the magnetic field but almost vertical leading to a slowly expending CR charge distribution in the upstream medium.

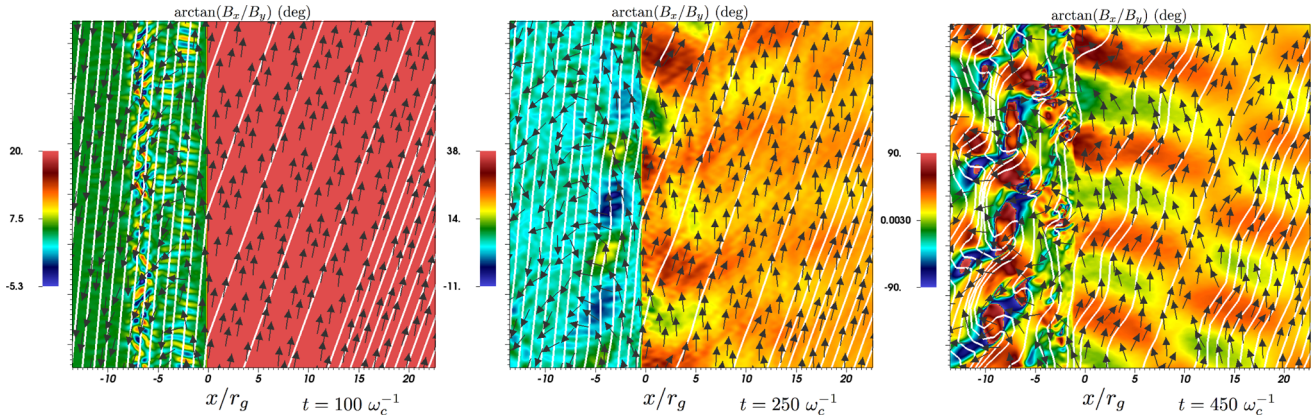

Figure 10. Temporal evolution of the magnetic field lines for the $M_A = 30$ oblique shock. The colour map represents the opening angle of the magnetic field lines in the x–y plane, while white lines stand as the magnetic field lines. Black arrows indicate the orientation of the CR current in the same plane. In such oblique configuration, the CR current is not parallel to the magnetic field as a drift motion is enforced by the electromotive field. The initial shock drift acceleration enables accelerated particles to flow in the upstream medium but does not trigger the NRS instability as the CR electrical current is slowly propagating in the upstream medium compared to a parallel shock configuration. The NRS instability eventually occurs in the downstream medium where a large wavelength magnetic perturbation leads to the corrugation of the shock hence triggering particle acceleration.

4.1.2 Corrugation of the shock front

The propagation of suprathermal particles in the upstream medium leads to a strong filamentary instability when the magnetic field is nearly parallel to the shock front normal. During the initial expansion of suprathermal particles in the precursor of the oblique shock, we do not observe any NRS instability features, apart from very small amplitude fluctuations in the magnetic field. Bell (2005) has presented a derivation of the dispersion relation of the instability for any obliquity of the magnetic field and stated that this instability can occur provided that the magnetic field is not perpendicular to the incoming flow. Reville & Bell (2012) completed the description of the instability by taking into account the back-reaction of the plasma upon the suprathermal particles in a parallel shock framework. In such context, one can summarize the whole instability process by considering the link between the suprathermal current and the potential vector component parallel to the flow, namely $J_{\rm part} \propto A_\parallel$. If a local maximum of $A_\parallel$ is met at some location, the magnetic force induced by suprathermal particles is pushing out the plasma material from the initial location hence expending the region where $A_\parallel$ is maximal. The related increase of the suprathermal current will then lead to a runaway process triggering the filamentation instability.

In an oblique shock context, the local physical conditions are quite different. Indeed obliquity angles θ_B larger than 45° leads to the aforementioned shock drift acceleration process when injecting particles near the shock front. Particles crossing the shock front to propagate in the precursor are selected through the SDA process. In order to counterbalance the drift motion induced by the local electromotive field, particles must have a sufficiently high velocity module and pitch angle. Such selection leads to a slowly expanding CR electrical current in the upstream medium. During the beginning of the simulation, this upstream electrical current does not reach a steady state conversely to the parallel shock case. This configuration differs from the framework of the linear analysis of Bell (2005) where a constant CR current over space and time is assumed. The varying current is likely to prevent a dominant wavelength to arise in the upstream medium so that no filamentary structure appears (see Fig. 13, upper left). In the meantime, downstream small amplitude magnetic variations can be seen in the close vicinity of the shock (Fig. 10). These fluctuations are induced by the streaming of the particle experiencing the SDA process.

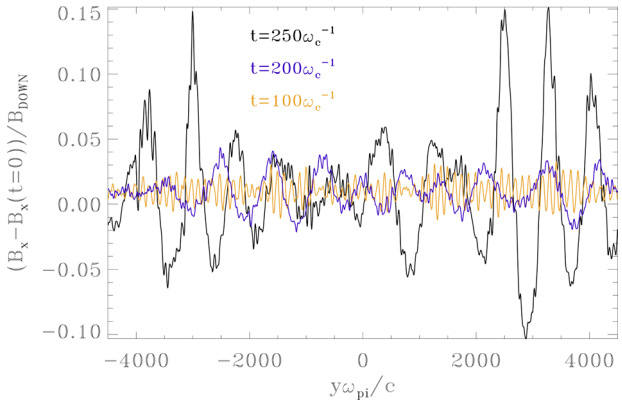

Figure 11. Variation of δB_x along the y-axis just behind the shock in the downstream region. Initially, small wavelength perturbations are present due to the SDA process at work at the shock. Later on, a large scale oscillation grows and dominates the entire magnetic structure leading to the corrugation of the shock. This large-scale modulation of the magnetic field is induced by a NRS instability triggered by the weak suprathermal electric current.

In the later phase of the simulation, a large-scale oscillation of the magnetic field arises just behind the shock in the downstream medium (see middle panel of Fig. 10). We display in Fig. 11 the average variation of B_x just behind the shock at three stages of the simulation. One can clearly see that as time goes by, a long wavelength oscillation occurs in the magnetic field (the same profile also applies to B_z). Such an oscillation unbalances the equilibrium of the shock front leading to a corrugation of the shock whose wavelength matches the one from the magnetic oscillation (see Fig. 12).

4.1.3 Particle acceleration near the corrugated shock

The corrugation of the shock affects the magnetic structure in its close vicinity. Indeed we can see in Fig. 10 that the opening angle of the magnetic field lines increases in some periodic locations along the shock front. Such bending of the field lines creates locally the physical conditions prevailing in near-parallel shocks, hence enabling a large number of particle to enter the upstream medium (see the left-hand panel of Fig. 12 where three channels of particle

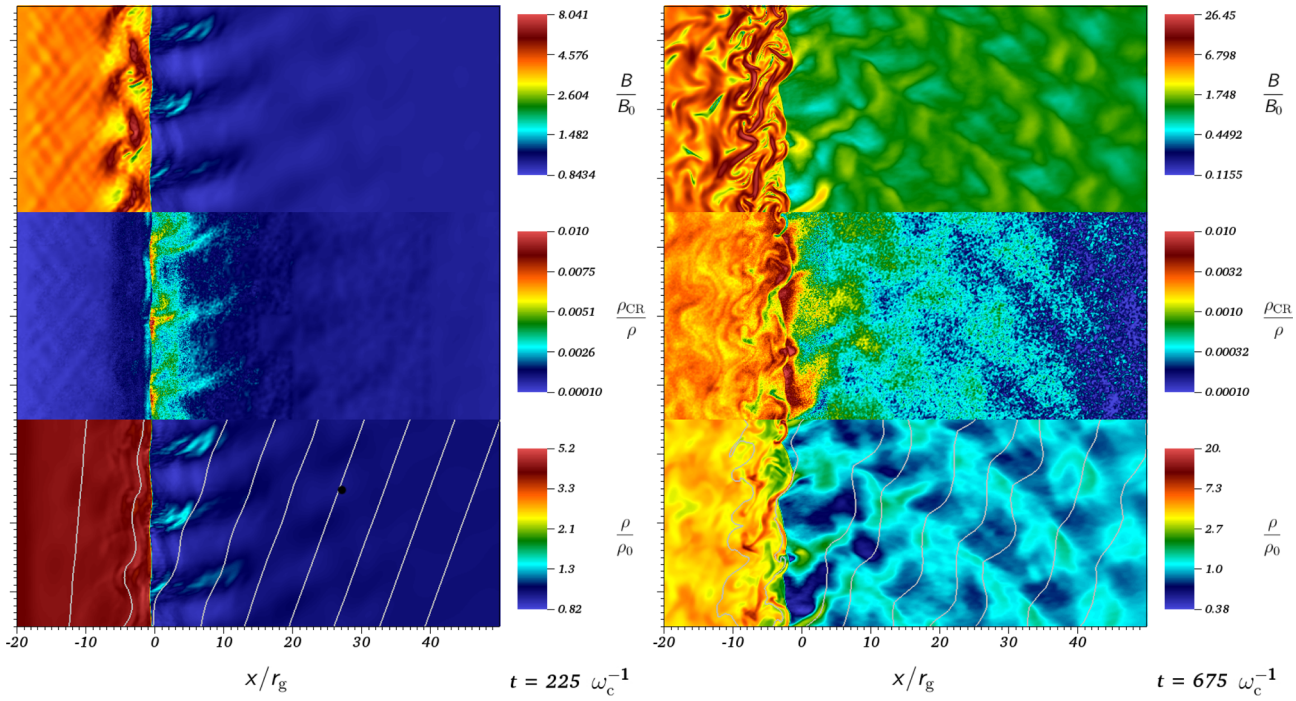

Figure 12. Similar to Figs 2 and 7, but with $M_A = 30$ and the angle between the magnetic field and the direction of the flow $\theta_B = 70^o$. These two snapshots exhibit the late stages of the oblique shock simulation where the corrugation of the shock front, induced by a NRS instability behind the shock, leads to particle acceleration as part of the shock display physical properties consistent with parallel-type shock configuration.

arise from the downstream medium to flow into the upstream). The massive input of particle triggers magnetic turbulence dominated by the corrugation wavelength. The contrast between early and late spectra is visible in Fig. 13 where we displayed the magnetic power spectrum of the B_x component for both early and late stages of the simulation.

In the early phase of the simulation, the upstream spectrum does not show any dominant pattern, while in the downstream spectrum, the weak magnetic fluctuations induced by the streaming of particle along the shock front are visible. In the late stages of the simulation, powerful magnetic fluctuations occur in both media whose dominant wavelength corresponds to the shock corrugation wavelength. Once strong turbulence is triggered, suprathermal particles experience a more chaotic motion regime leading to a diffusive shock acceleration process.

The energy spectrum of the particles at various times is displayed in Fig. 14. During the early phase, the energy particle distribution is consistent with SDA spectrum where numerous particles get accelerated up to 10 times their injection energy, while the majority of these particles gets decelerated due to their interaction with the ambient plasma and magnetic field. The energy spectrum remains the same until $t \sim 200\omega_c^{-1}$ when an additional tail appears due to the interaction between the particles and the shock. This tail converges towards a $f(E) \propto E^{-3/2}$ distribution consistent with a diffusive shock acceleration process. It is noteworthy that the maximal energy reached by suprathermal particles is approximately $300E_{inj}$, namely 10 times the maximal energy obtained in the parallel shock simulation. Such result is consistent with the combined effect provoked by SDA and DSA.

4.1.4 Origin of the shock corrugation

The corrugation of the shock front appearing in our simulations has not been observed in previous full-PIC or hybrid computations (see Section 5 for a comparison with previous studies). In order to make sure that this phenomenon is genuinely physical we have performed a series of test and analysis. First of all, computing the suprathermal particle current density enables us to compare the large-scale wavelength fluctuation occurring downstream of the shock to the predicted dominant mode that would be generated by the NRS instability in the downstream medium. Usually, this instability does take place in the upstream region as it displays a larger Alfvénic Mach number, hence allowing a wider range of unstable mode to arise. In the context of a highly oblique shock, the upstream NRS instability is not triggered whereas it can in the downstream medium where the CR current reaches a steady state more rapidly as no selection through the SDA process is required for downstream particles.

The set-up of our simulation leads to a downstream medium where the Alfvénic Mach number remains larger than 1 ($M_A \sim 4$). The downstream suprathermal particle current rapidly decreases away from the shock (see Fig. 13). Computing the average value of the current leads to a ratio $J_{part}c/\omega_{pi}B_{down}$ of the order of 0.018. Such a ratio is consistent with a dominant unstable mode whose wavelength is $\lambda \sim 720c/\omega_{pi} = 8r_g$. This is consistent with the wavelength observed in the magnetic fluctuation (see Fig. 11). On the other hand, the characteristic growth time-scale in such conditions is $t_{gr,max} = \omega_{pi}B_{down}/J_{part}c\omega_c^{-1} \simeq 50\omega_c^{-1}$. The growth time-scale is quite large but consistent with the fact that we do see the rise of the corrugating magnetic fluctuation after at least $200\omega_c^{-1}$ (see Fig. 11).

At this point we have performed a series of tests in order to ensure that the corrugation of the shock does not result from any numerical artefact. To that end, we have run a simulation where we have increased the y extension of the computational domain by a non-integer number, namely 2.5. In addition to that modification, we have also turn-off the AMR procedure and set the resolution of the uniform grid to the highest spatial resolution used in AMR computations. We have recovered, using the same initial

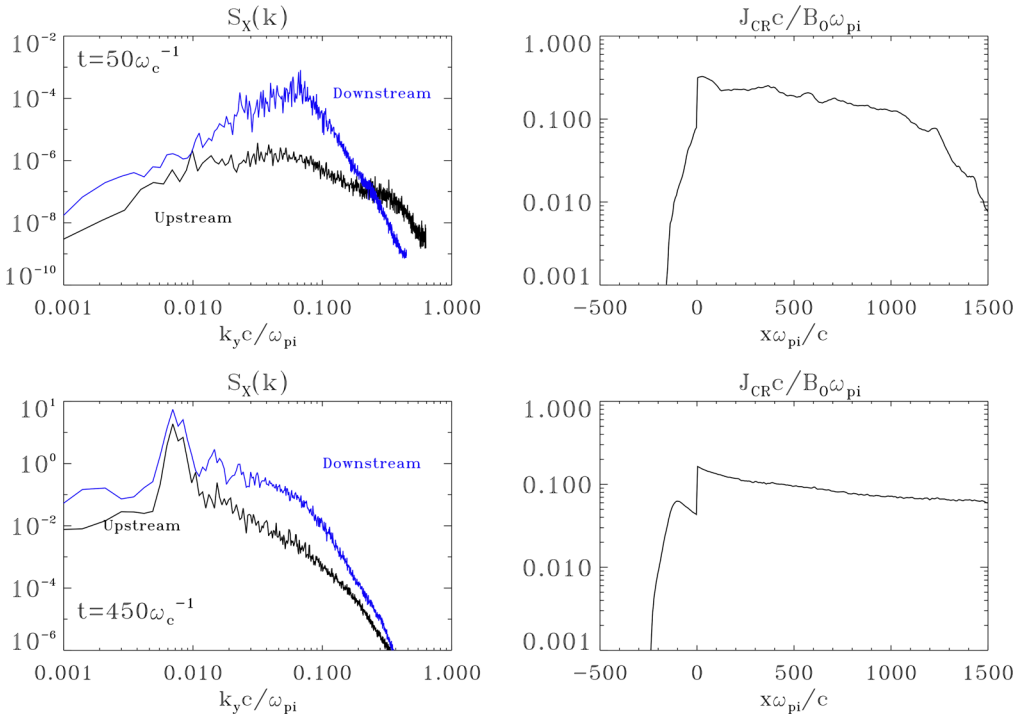

Figure 13. Upstream and downstream magnetic power spectrum of the magnetic field component parallel to the flow in (left) an early phase and in a (right) later stage of the simulation. In the early phase the upstream medium exhibits no dominant mode showing that the NRS instability is not triggered despite the presence of an upstream current. We do see however fluctuations in the downstream medium related to the injected particle being process through SDA as fluctuations occur just behind the shock front. In the later phase of the simulation a large wavelength mode is visible in both the downstream and upstream magnetic spectra. Such large wavelength oscillation does correspond to the corrugation wavelength of the shock and is induced by a NRS instability occurring in the downstream medium. The small current present just behind the shock are shown on the right-hand column.

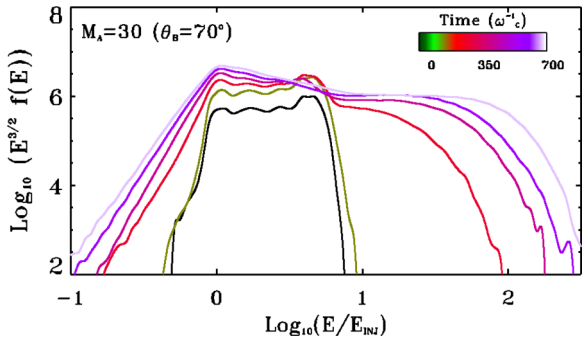

Figure 14. Energy spectra of non-thermal particles injected at energy $E_{\rm inj}/mc^2 = 4 \times 10^{-5}$. The various spectra correspond to simulations displayed in Fig. 10.

conditions, exactly the same corrugation phenomenon with the same wavelength and particle spectrum. Such results comforted us that the corrugation of the shock is not induced by the set-up of the computation domain nor its spatial extension. We then turn our attention to the injection procedure of the particles. We have done another series of runs where we have modified the charge of the particle or their mass, hence modifying the Larmor radius of the injected particles. It turns out that in computation where we only changed the mass but not the charge of the particles, we recover the same corrugation pattern with the same wavelength. On the other hand, when changing the charge of the particle while leaving untouched their mass, we recover the corrugating pattern but with a different wavelength proportional to the change in the electrical charge of the particle. These computations then prove that the origin of the corrugating pattern is only dependent on the suprathermal particle current and not on the particle Larmor radius. Such result rules out the resonant streaming instability and proves that the NRS instability is very likely the mechanism at the origin of the corrugation of the shock.

Finally, we also mention that no particle acceleration and no shock corrugation have been observed in a strictly perpendicular shock at times as long as $1000\omega_{\rm c}^{-1}$.

4.2 Higher Alfvénic Mach number simulations

Fig. 15 shows what happens when we combine a higher Alfvénic Mach number ($M_{\rm A} = 300$) shock with a magnetic field that makes a 70° angle with the direction of motion. Initially, particle acceleration occurs in a similar fashion as for the $M_{\rm A} = 30$ case, namely through a SDA mechanism. We eventually also observe a corrugating shock front on the same time-scale than in the $M_{\rm A} = 30$ simulation. It is important to mention here that in order to have an upstream Mach number $M_{\rm A} = 30$ we increased the velocity of the shock by a factor of 10. Accordingly, we have increased the injected particle velocity $v_{\rm inj}$ by a factor of 10 so that the fiducial length and time, $\omega_{\rm c}^{-1} \propto v_{\rm inj}^{-1}$ and $r_{\rm g} \propto v_{\rm inj}$, are also changed. Keeping the same injection recipe leads to a similar downstream suprathermal current that is still in agreement with the observed corrugation wavelength. This result suggests that the NRS instability is indeed the mechanism at work in the corrugation of the shock front.

However, we do observe some effect of the Mach number on the upstream medium. On top of the patterns that we found in the

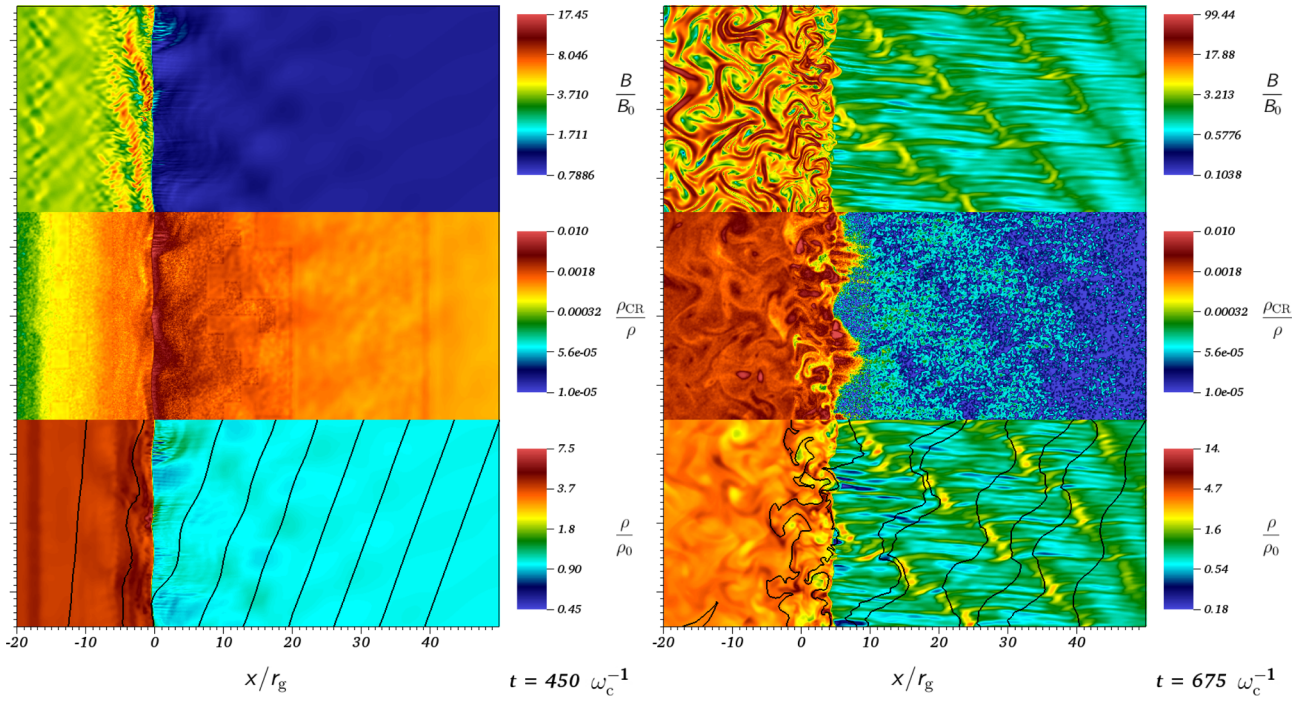

Figure 15. Similar to Figs 12 and 7, but for $M_A = 300$ and $\theta_B = 70°$. Although the large-scale instabilities in the upstream medium are similar to the $M_A = 30$ case, they show a far more elongated pattern as a result of the higher Mach number.

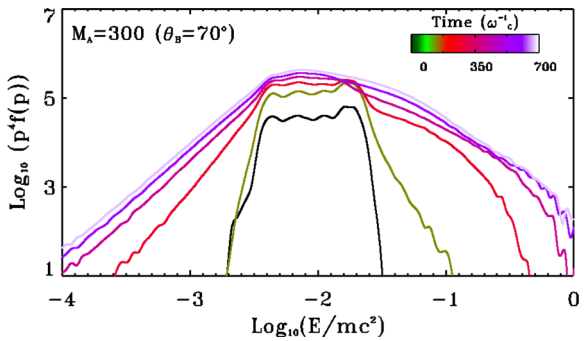

Figure 16. Energy spectra of non-thermal particles injected at energy $E_{inj}/mc^2 = 4 \times 10^{-3}$ near a $M_A = 300$ shock. The various spectra correspond to simulation displayed in Fig. 15. It is noteworthy that some suprathermal being accelerated through a combined SDA–DSA process are able to reach the relativistic regime (with Lorentz factors of the order of a few units).

$M_A = 30$ case, we see a second instability that creates filament along the incoming flow. We do believe that this is the result of the high flow speed, which prohibits any significant motion perpendicular to the direction of the flow hence dislocating the transverse filamentation occurring once the shock is fully corrugated (see right-hand panel of Fig. 15). The energy spectrum of the suprathermal particles in the $M_A = 300$ simulation is displayed in Fig. 16 . The shape of the spectrum is nearly identical to the $M_A = 30$ case, namely an initial pile-up of accelerated particle through SDA completed afterwards by a higher energy tail associated with a DSA process. It is noteworthy that in this simulation the injected non-relativistic particles are able to reach a (moderate) relativistic regime as the Larmor radius of the most energetic particles is of the order of a few units.

5 DISCUSSION

Our parallel shock model succeeds in reproducing earlier results obtained with both a dihybrid code (e.g. Caprioli & Spitkovsky 2014a) and a combined PIC–MHD code (Bai et al. 2015). They also confirm the theoretical predictions for NRS instabilities by Bell (2004, 2005). While performing these simulations we also tested the effect of varying the angle between the flow and the magnetic field and find results similar to those of e.g. Caprioli & Spitkovsky (2014a) for small angles (up to approximately 45°). In contrast, the oblique shock model shows a new, unexpected result, which deviates considerably from the results obtained previously by Caprioli & Spitkovsky (2014a). It is noteworthy that such simulations have never been done using a PI[MHD]C code so direct comparison is impossible. In Section 4 we have discussed the mechanisms that lead to the formation of instabilities in both the upstream and downstream medium when the magnetic field makes a large angle with the direction of the flow. We should note here that when we increase the angle even further beyond 70° this effect disappears since the component of the particle velocity parallel to the flow becomes smaller than the drift velocity if the thermal plasma, which eliminates the upstream current. The question remains as to why this result was not obtained with a hybrid code. By comparing our simulations with these earlier models we come to the conclusion that there are two factors that contribute to the different outcome.

(i) *The number of particles*. Although the absolute number of particles used in hybrid codes is far larger than what we use for the PI[MHD]C simulations, only a small fraction of the particles in hybrid simulations actually are suprathermal. Combined with the fact that for an oblique magnetic field only a fraction of the non-thermal particles are able to move upstream because of their pitch angle, we conclude that the hybrid simulations lacked the necessary number of particles to create the current that causes the disturbance of the upstream magnetic field.

(ii) *The size of the physical domain*. The size of the simulated domain in the direction perpendicular to the shock-normal is six times larger in our model than in the original hybrid simulation. This allows us to capture the long wavelength that corrugates the shock and sets in motion the process that disturbs the upstream magnetic field. The smaller domain used by the hybrid simulation makes this impossible. We have tested our code with a physical domain similar to that used by Caprioli & Spitkovsky (2014a) and find that indeed the long wavelength never appears and so is the magnetic field amplification.

These points demonstrate the opportunity that the PI[MHD]C method affords us. Because it is designed primarily to simulate large-scale structures, is less computationally expensive than PIC or hybrid methods and enables us to run the simulation in the frame of reference of the shock, it allows us to simulate a large volume of space, using a larger number of suprathermal particles, which in this particular case proved to be necessary.

2D3V PIC simulations of perpendicular and oblique shock configurations have been performed by Kato & Takabe (2010) and Wieland et al. (2016), respectively. These studies verify that fast Alfvénic Mach (low magnetization) number shocks are mediated by the Weibel instability. These studies only report on electron thermalization but find pieces of evidence for the development of a proton non-thermal tail possibly connected with a shock surfing process in the perpendicular shock configuration. We confirm with Caprioli & Spitkovsky (2014a) that protons are accelerated at oblique shocks with an angle $\theta_B = 45^\circ$. However, we argue that particle acceleration also proceeds at larger angles through the two-steps instability process described in Section 4 as identified by Reville & Bell (2013). But we do not observe any acceleration at perpendicular shocks at the time-scales explored in the simulations.

Ideally, we would like to go for a long PIC or a hybrid simulation to be run in order to verify our results. However, such a simulation would require considerable computational resources. The simulation box would have to be large enough along the axis parallel to the flow to be able to follow the shock for a time frame of at least $400\,\omega_c^{-1}$ to capture both the formation of the long wavelength pattern in the upstream medium and the response of the shock and downstream medium to this development. Along the perpendicular axis it would need to be large enough to capture the long wavelength. Finally, the number of particles would have to be increased, not only to compensate for the larger volume, but also to provide sufficient suprathermal particles to reproduce the upstream current.

It should be kept in mind that we are using a 2D model to investigate what is fundamentally a 3D problem. We have chosen to do so in order to limit the computational cost of our simulations and to reproduce the existing 2D models for purpose of comparison. The non-resonant streaming instability is an inherently 3D phenomenon. Reducing it to 2D is likely to alter its growth and encourages the formation of filaments in the upstream medium, rather than a true 3D structure.

6 CONCLUSIONS

Our simulations prove that our code can reliably reproduce earlier work (Bai et al. 2015) and analytically predicted effects. We recover the ignite of the NRS in the parallel shock configuration that further produces a filamentation of the upstream plasma. Particle acceleration takes place due to the DSA mechanism. In the oblique shock configuration we also find the development of magnetic field amplification and particle acceleration. But these occur in a two-step process: first particle are accelerated by SDA and gain energy up to nine times the injection energy. This induces in turn a CR current able to trigger the NRS instability downstream that finally leads to a strong shock corrugation. At locations along the shock front where the magnetic field is sufficiently perturbed to retrieve a quasi-parallel configuration bunches of CR are able to explore the upstream medium and trigger a NRS instability and a filamentation of the medium as in the parallel shock case. Once the NRS instability is onset particles start to gain energy under the effect of DSA. Maximum particle energies at the same time-scales are found to be higher in the oblique configuration with respect to parallel shock case.

The simulations prove that for any kind of astrophysical shock, the particle acceleration and magnetic field amplification play an important part in determining the characteristics of the shock. We stop our simulations at 675 gyrotimes. Assuming that the magnetic field equals 5×10^{-6} G (typical for interstellar magnetic fields), this means that for the $M_A = 30$ case, approximately 1.5×10^4 s have passed. For the $M_A = 300$ case, it is 1.5×10^5 s. Both times are short compared to the typical lifetime of circumstellar and interstellar shocks. Clearly, the presence of non-thermal particles start to influence the behaviour of a shock almost as soon as it is formed.

However, this study is quite preliminary in the sense it is 2D3V in dimensions. 3D simulations are mandatory to explore further the efficiency of the NRS instability. At present only non-thermal proton transport has been considered, our next study will also include electrons. For this we are adding a module calculating radiative losses (synchrotron, inverse Compton). Our study needs also to be extended to the case of relativistic flows. Both developments are foreseen to be delivered in a forth coming study.

ACKNOWLEDGEMENTS

We are grateful for fruitful regular discussions with A. R. Bell, C. A. Bret, A. Bykov, M. Dieckmann, E. D'humières, M. Grech, L. Gremillet, R. Keppens, B. Lembège, M. Lemoine, G. Pelletier, I. Plotnikov and V. Tikhonchuk. This work is supported by the ANR-14-CE33-0019 MACH project. We would like to thank D. Caprioli and B. Reville for helpful comments. We also thank our anonymous referee for helpful comments and suggestions. This work acknowledges financial support from the UnivEarthS Labex program at Sorbonne Paris Cité (ANR-10-LABX-0023 and ANR-11-IDEX-0005-02). This work was granted access to HPC resources of CINES under the allocation A0020410126 made by the Grand Equipement National de Calcul Intensif (GENCI).

REFERENCES

Bai X.-N., Caprioli D., Sironi L., Spitkovsky A., 2015, ApJ, 809, 55
Balsara D. S., Spicer D. S., 1999, J. Comput. Phys., 149, 270
Bell A. R., 1978, MNRAS, 182, 147
Bell A. R., 2004, MNRAS, 353, 550
Bell A. R., 2005, MNRAS, 358, 181
Bell A. R., Schure K. M., Reville B., Giacinti G., 2013, MNRAS, 431, 415
Berezhko E. G., Ellison D. C., 1999, ApJ, 526, 385
Birdsall C. K., Langdon A. B., 1991, Plasma Physics via Computer Simulation. IoP Publishing, Bristol
Caprioli D., Spitkovsky A., 2013, ApJ, 765, L20
Caprioli D., Spitkovsky A., 2014a, ApJ, 783, 91
Caprioli D., Spitkovsky A., 2014b, ApJ, 794, 46
Caprioli D., Pop A.-R., Spitkovsky A., 2015, ApJ, 798, L28
Decker R. B., 1988, Space Sci. Rev., 48, 195
Drury L. O., 1983, Rep. Progress Phys., 46, 973

Ferrell R., Bertschinger E., 1994, Int. J. Modern Phys. C, 5, 933
Kato T. N., Takabe H., 2010, ApJ, 721, 828
Lucek S. G., Bell A. R., 2000, MNRAS, 314, 65
Marcowith A. et al., 2016, Rep. Progress Phys., 79, 046901
Parizot E., Marcowith A., Ballet J., Gallant Y. A., 2006, A&A, 453, 387
Reville B., Bell A. R., 2012, MNRAS, 419, 2433
Reville B., Bell A. R., 2013, MNRAS, 430, 2873
Reville B., O'Sullivan S., Duffy P., Kirk J. G., 2008, MNRAS, 386, 509
Riquelme M. A., Spitkovsky A., 2010, ApJ, 717, 1054
Shephard M. S., Georges M. K., 1991, Int. J. Numer. Methods Eng., 32, 709
Vainio R., Schlickeiser R., 1998, A&A, 331, 793
van der Holst B., Keppens R., Meliani Z., 2008, Comput. Phys. Commun., 179, 617
Wieland V., Pohl M., Niemiec J., Rafighi I., Nishikawa K.-I., 2016, ApJ, 820, 62
Zachary A. L., Cohen B. I., 1986, J. Comput. Phys., 66, 469
Zirakashvili V. N., Ptuskin V. S., Völk H. J., 2008, ApJ, 678, 255

SUPPORTING INFORMATION

Supplementary data are available at *MNRAS* online.

M30_70degrees_movie.mpg
M30_parallel_movie.mpg

Please note: Oxford University Press is not responsible for the content or functionality of any supporting materials supplied by the authors. Any queries (other than missing material) should be directed to the corresponding author for the article.

APPENDIX A: ANIMATIONS

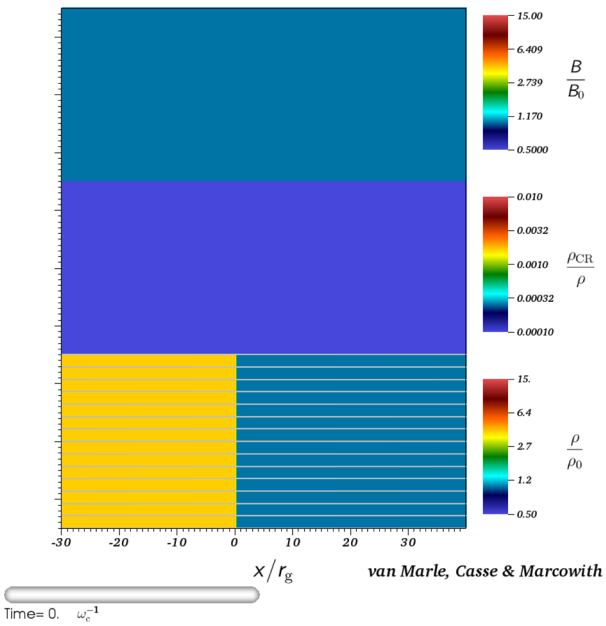

Figure A1. In this animation of a parallel shock with $M_A = 30$ we show the evolution of the magnetic field strength relative to the original magnetic field (top), non-thermal particle charge density relative to the thermal gas density (middle) and thermal gas mass density relative to the upstream density at the start of the simulation, combined with the magnetic field stream lines (bottom). The gas is streaming through the shock from right to left. Over time suprathermal particles are introduced at the shock, causing instabilities in the thermal gas.

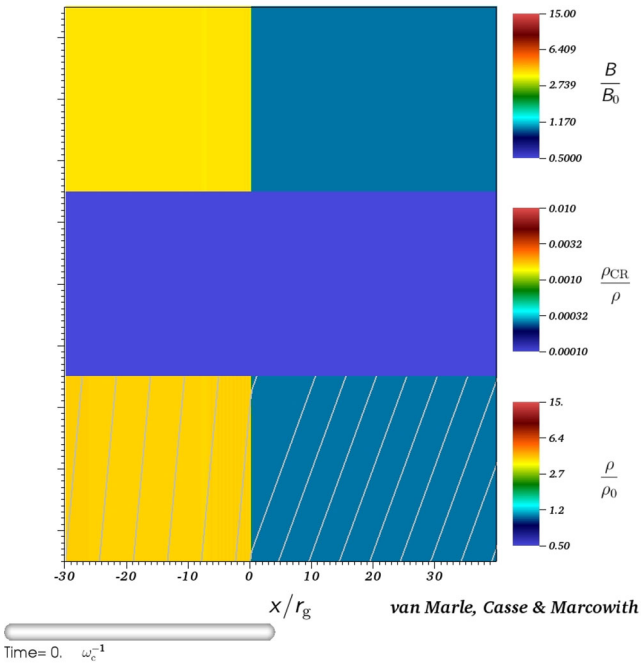

Figure A2. Similar to Fig. A1, but for the simulation with $M_A = 30$ and $\theta_B = 70^o$. The animation clearly demonstrates the appearance of the long wavelength pattern in the upstream gas.

This paper has been typeset from a TEX/LATEX file prepared by the author.